NANO · MICRO small
www.small-journal.com

# Cathode Interface Construction by Rapid Sintering in Solid-State Batteries

*Jinhang Chen, Weiyin Chen, Bing Deng, Bowen Li, Carter Kittrell, and James M. Tour**

**Solid-state batteries (SSBs) are poised to replace traditional organic liquid-electrolyte lithium-ion batteries due to their higher safety and energy density. Oxide-based solid electrolytes (SEs) are particularly attractive for their stability in air and inability to ignite during thermal runaway. However, achieving high-performance in oxide-based SSBs requires the development of an intimate and robust SE–cathode interface to overcome typically large interfacial resistances. The transition interphase should be both physically and chemically active. This study presents a thin, conductive interphase constructed between lithium aluminum titanium phosphate and lithium cobalt oxide using a rapid sintering method that modifies the interphase within 10 s. The rapid heating and cooling rates restrict side reactions and interdiffusion on the interface. SSBs with thick composite cathodes demonstrate a high initial capacity of ≈120 mAh $g^{-1}$ over 200 cycles at room temperature. Furthermore, the rapid sintering method can be extended to other cathode systems under similar conditions. These findings highlight the importance of constructing an appropriate SE–cathode interface and provide insight into designing practical SSBs.**

## 1. Introduction

The demand for safer energy storage systems in portable electronics and electric vehicles has led to the development of next-generation rechargeable battery technologies beyond current lithium-ion batteries (LIBs). With the rapid emergence of various types of solid electrolytes (SEs) with high conductivity and thermal stability, solid-state batteries (SSBs) have the potential to alleviate common safety problems in LIBs by replacing organic liquid electrolytes with nonflammable SEs.[1,2] Inorganic SEs, including oxides and sulfides, are considered good candidates due to their high ionic conductivities.[3,4] Sulfide SEs have attracted much attention for their higher conductivity ($10^{-3}$ to $10^{-2}$ S $cm^{-1}$) and ease of synthesis.[5–8] However, a narrow electrochemical window and poor chemical stability against Li metal limit their performance in practical applications. The sensitivity to moisture and oxygen hinders their mass production at a competitive cost.[9] Oxide-based SEs (denoted as O-SE) possess good ionic conductivity (≈$10^{-3}$ S $cm^{-1}$) and good electrochemical stability at high voltages.[10] Among O-SEs, lithium aluminum titanium phosphate ($Li_{1.3}Al_{0.3}Ti_{1.7}(PO_4)_3$, LATP, NASICON-type)[11–14] and lithium lanthanum zirconium oxide ($Li_7La_3Zr_2O_{12}$, LLZO, garnet-type)[15–17] have been widely investigated. LATP is chemically stable in the air while LLZO reacts with $H_2O$ and $CO_2$ to form an insulating LiOH and $Li_2CO_3$ layer.[18] The development of high-performance SSBs is highly dependent on the composition of SEs, fabrication, and modifications made to the interface.[19–21] For oxide-based SSBs (denoted as O-SSBs), extensive research has been conducted on the anode interface between lithium metal and O-SEs. Effective methods such as surface treatment, interface layer coating, and alloying stabilize Li metal and suppress dendrite growth.[22–26] Additionally, the surface modification method can efficiently protect LATP from $Ti^{4+}$ reduction.[27–29] However, direct contact between SEs and the cathode active materials remains a bottleneck in the development of O-SSBs.[30–34] Intimate physical contact and low impedance for $Li^+$ transfer are crucial factors for efficient cathode interface construction. The rigid nature of oxide ceramics causes a point-to-point contact to the active materials; gaps and voids form after experiencing volume changes during cycling. In addition to physical contact, chemical interaction is also essential in creating a pathway for $Li^+$ transfer. The lattice mismatch between cathode materials and O-SEs introduces space-charge regions due to the deficiency of cations and anions at the interface.[35]

## 2. Results and Discussion

### 2.1. Design of the Oxide SE Solid-Phase Sintering

The sluggish transfer kinetics in oxide based SSBs are attributed to high interfacial resistance at the cathode interface. Previous

J. Chen, W. Chen, B. Deng, B. Li, C. Kittrell, J. M. Tour
Department of Chemistry
Rice University
6100 Main Street, Houston, TX 77005, USA
E-mail: tour@rice.edu
J. M. Tour
Department of Materials Science and NanoEngineering
Smalley-Curl Institute
Nanocarbon Center and the Rice Advanced Materials Institute
Rice University
6100 Main Street, Houston, TX 77005, USA

The ORCID identification number(s) for the author(s) of this article can be found under https://doi.org/10.1002/smll.202307342

**DOI: 10.1002/smll.202307342**

 

attempts to improve the physical contact between the SE and the cathode include incorporating polymers into the SE framework. These $Li^+$-conductive polymers fill the gap between the SE and cathode, thereby increasing the contact area and ionic conductivity.[36–38] However, such a polymer-containing design can reduce the thermal stability of the SSBs. A thin layer of materials like Nb, $Al_2O_3$, and $LiCoO_2$ induced by pulsed layer deposition can facilitate $Li^+$ transfer at the interface.[39–41] Currently, this method remains expensive and is not available for a high mass loading electrode. An alternative approach to treat the cathode interface is co-sintering, which allows for modifications of both physical contact and chemical interaction. Researchers have studied the reactivity between O-SEs, such as garnet and NASICON, and common cathode active materials, such as $LiCoO_2$ (LCO), $LiFePO_4$ (LFP), or $LiNi_xMn_yCo_{1-x-y}O_2$ (NMC), at different sintering temperatures.[42–45] From ≈550 °C, which is much lower than the ≈700 °C temperature required to form intimate physical contact, side products such as $LiCoPO_4$, $TiO_2$, $Co_3O_4$, and $Li_3PO_4$ are identified. Although intimate physical contact is observed on the interface at high co-sintering temperatures, the interface was not chemically active for $Li^+$ transfer. Reactions between O-SEs and oxide cathodes during annealing degrades the interfacial properties and limits the temperature range of co-sintering. Various $Li^+$ non-conductive compounds form in the process. Kim et al. reported the onset temperatures for LCO and LFP cathodes are ≈600 and ≈500 °C, respectively.[46] In addition, during the co-sintering process, serious Li loss and element interdiffusion also occurs on the electrode, which further reduces the capacity of the SSBs. $Li_3BO_3$ and $B_2O_3$ have been introduced as "liquid-phase" sintering aids since they melt and fill the pores in the particles and enable intimate contact between the SE and cathode. The formed $Li_3BO_3$ interphase offers a $Li^+$ conductivity of $10^{-6}$ S $cm^{-1}$, as demonstrated by the Goodenough group.[47] The sintering temperature was successfully lowered to 700 °C to reduce side reactions. Another study suggests 1% $B_2O_3$ addition can reduce the sintering temperature from 800 to 640 °C under high pressure for 2 min in the spark plasma sintering technique.[48] The decomposition of LCO is avoided at the lower sintering temperature and a record-high areal capacity was achieved. However, the lower $Li^+$ conductivity of the borate layer (≈$10^{-5}$ S $cm^{-1}$) likely hindered the charge rate and capacity of the cathode materials,[49] which makes the performance of SSBs unsatisfactory at room temperature or requires a small amount of liquid electrolyte to be added. In the conventional co-sintering studies of O-SSBs, high temperature and long duration are used to achieve an intimate contact. Hu et al. reduced the resistance between garnet and $V_2O_5$ by rapid annealing of the device at ambient pressure under Ar. Melted $V_2O_5$ wets the solid electrolyte at 550 °C.[50]

In this study, we demonstrate the effectiveness of rapid sintering strategies in the fabrication of thick LCO composite cathodes (Figures S1 and S2, Supporting Information). No obvious degradation of oxide cathodes was observed after a fast, high-temperature thermal treatment. The interfacial resistance was significantly reduced. LATP was selected as the solid electrolyte because it offers moderate ionic conductivity and good stability in air. We investigated the reactivity between LATP and various commercially available cathode materials. The reaction to form a conductive interphase was limited to the surface, while the bulk cathode remained stable. Unlike the thin-film slurry coating process in LIBs, this rapid sintering process was done in the solid phase. Cathodes sintered in a furnace were also tested and compared. This rapid sintering improved the density and conductivity of the solid electrolyte, and no additional liquid electrolyte was added between the cathode and SE. The SSBs with co-sintered cathodes could be reversibly charged and discharged at room temperature.

### 2.2. Rapid Sintering of LCO-LATP Cathode

The synthesis of the LATP in a furnace is described in the Experimental Section. The synthesized LATP powder matched well with the X-ray diffraction (XRD) patterns of $LiTi_2(PO_4)_3$ (Figure S3, Supporting Information). A portion of the LATP powder was cold-pressed and rapid sintered at 980 °C for 20 s into a LATP pellet. The rapid sintered LATP has a moderate ionic conductivity of $5.4 \times 10^{-4}$ S $cm^{-1}$ measured at 25 °C (Figure S4, Supporting Information). No obvious decomposition or $Li_2CO_3$ layer formation on the solid electrolyte was observed in XRD patterns after the rapid sintering (Figure S5, Supporting Information).

The fabrication process for LCO-LATP composite cathodes is shown in **Figure 1**a. To achieve a thick cathode layer, the composite cathode layer was composed of LCO as well as LATP powder and conductive carbon black for ionic and electronic conductivity. The cathode mixture was sprayed on the LATP powder to ensure intimate particle contact, and the mixture was cold pressed into a monolithic pellet (≈160 MPa). The compressed composite cathode was placed into the space between two carbon papers connected to electrodes (Figure S1, Supporting Information) and heated to the target temperature (see details in Experimental Section). A precise temperature control was achieved in different trials (Figure S2, Supporting Information). The rapid sintering device provides stable and high-energy output with voltages up to 63 V.[50,51] The rapid sintering temperature from 700 to 1000 °C was further controlled by varying the resistance of the carbon paper sheets (Figure 1b). The emission spectrum of the reaction was recorded by an infrared thermometer to acquire the temperature curves. The heating duration was programmed to be 5 s and two pulses were applied. The rapid heating and cooling rates enabled a fast thermal treatment. The rapid sintering process can be carried out in air since LATP possesses high stability against $CO_2$ when compared to a garnet solid electrolyte. With the rapid sintering device, LATP and LCO-LATP composite pellets are annealed within 10 s. Their density and mechanical strength are greatly enhanced. Digital and scanning electron microscopy (SEM) images of sintered pellets are shown in Figure 1c–f. The LATP pellet (Figure 1c) showed a high relative density of 95% and a large grain size (Figure 1d). X-ray diffraction (XRD) powder patterns of synthesized and commercial LATP are in good agreement (Figure S3 Supporting Information). Electrochemical impedance spectroscopy (EIS) of the LATP symmetric cell, tested at 25°C, is shown in Figure S4 (Supporting Information). XRD powder patterns of rapid-sintered LATP pellets (980 °C for 20 s) are shown in Figure S5 (Supporting Information). The high-resolution transmission electron microscopy (HRTEM) image (Figure S6, Supporting Information) indicates a high crystallinity of as-obtained LATP. The interplanar spacings of nanocrystalline grains of 0.42 and 0.60 nm correspond to (104) and (012) lattice

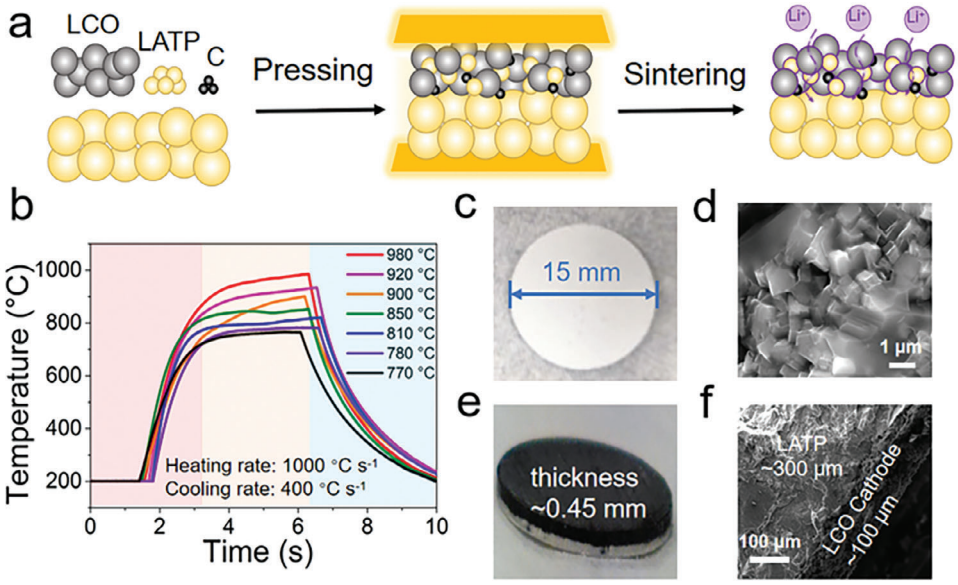


**Figure 1.** a) Schematic diagram of cathode preparation and rapid sintering procedure. b) Temperature measurement curves during the rapid sintering process. c) Digital and d) SEM images of rapid sintered LATP solid electrolyte pellet. e) Digital and f) SEM images of rapid sintered LATP/LCO-LATP double-layer pellet.

planes of LATP, respectively. In LCO-LATP pellets (Figure 1e), the two layers merged into a monolith with good physical contact after the thermal treatments. The thickness of LATP and cathode layer can be controlled at 200 to 300 μm and ≈100 μm, respectively (Figure 1f). This solid-phase rapid sintering reaction leads to the combination of the SE and the cathode composite layers without any liquid electrolyte addition.

Taking a pure LATP sintered pellet, cathode composite powder was sprayed and pressed onto its surface and a second pulse was applied on the carbon paper to heat the coated LATP pellet to 700–980 °C. After the treatment, the adhesion between the LATP layer and mixed cathode layer was greatly enhanced, which suggests grain boundary growth between LATP and mixed cathode particles. Unlike the point-to-point contact between pristine LCO and LATP particles, continuous, joined regions on the edges appeared in the sintered LATP-mixed cathode pellets. This is validated by SEM images before and after rapid sintering (Figure S7, Supporting Information). The LATP is more porous in the cathode layer compared to the dense pure LATP layer due to the short rapid sintering duration. The dense LATP layer separates Li metal from the LATP-LCO cathode and facilitates $Li^+$ transfer as the bulk electrolyte. The less dense LATP in the cathode layer enables better contact with the LCO particles and reduces crack formation after volume changes during cycling.

### 2.3. Temperature-Dependent Interphase Formation of LATP-LCO Composite Cathodes

Cathode decomposition and interphase formation are strongly related to the sintering temperature and duration. Further investigations of the reaction conditions of rapid sintering were made to determine the possible interphases between LCO and LATP in the mixed cathode layer. The phase stability of LATP and LCO was predicted by density-functional theory (DFT) calculations. A negative Gibbs free energy change suggests the reaction is highly thermodynamically favorable at various molar ratios.[48] Previous studies suggest that the crystalline domain size of LCO and LATP decrease at 300–500 °C and LCO starts to react with LATP to form $Li_2O$, $Li_3PO_4$, and $Co_3O_4$ at temperatures >600 °C.[42,45] This reactivity was confirmed with furnace sintering experiments. The composite cathode in this experiment was composed of LCO, LATP and acetylene black (AB) with a mass ratio of 70:27:3. The function of AB powder is to increase the electrical conductivity of the cathode. The resulting composite cathode pellet was heated in the furnace at 580, 640, or 700 °C for 1 h before the characterizations. SEM images of the furnace sintered cathode pellets suggests that physical contact between the LCO and LATP particles began at 640 °C. Sintering at 700 °C introduced grain growth, which provides close contact (Figure S8, Supporting Information). However, the XRD pattern revealed the formation of $Li_3PO_4$ and $Co_3O_4$ side products at 640 °C while the same side products also accumulated at 700 °C (**Figure 2**a). No obvious side products are identified at lower sintering temperatures. Single-phase LCO by itself is thermally stability in air up to 900 °C.[52] The reaction between LCO and LATP leads to LCO decomposition at a lower temperature.[42,45]

For comparison, additional LCO, LATP and AB composite cathode pellets were annealed under rapid sintering conditions. The temperature increased to the target temperature in ≈1 s (Figure 1b). The rapid sintering procedure was carried at 700, 850, or 980 °C and the XRD pattern was acquired of each rapid sintered pellet. No obvious side product was detected at 700 and 850 °C (Figure 2b). However, LATP and LCO intensity was greatly reduced at 980 °C. This is due to side reactions both at the interface and in the bulk particles. $Li_3PO_4$ and $Co_3O_4$ were identified as the major side products, like the pellets sintered in the furnace. The pellets became olive-green in color likely due to the

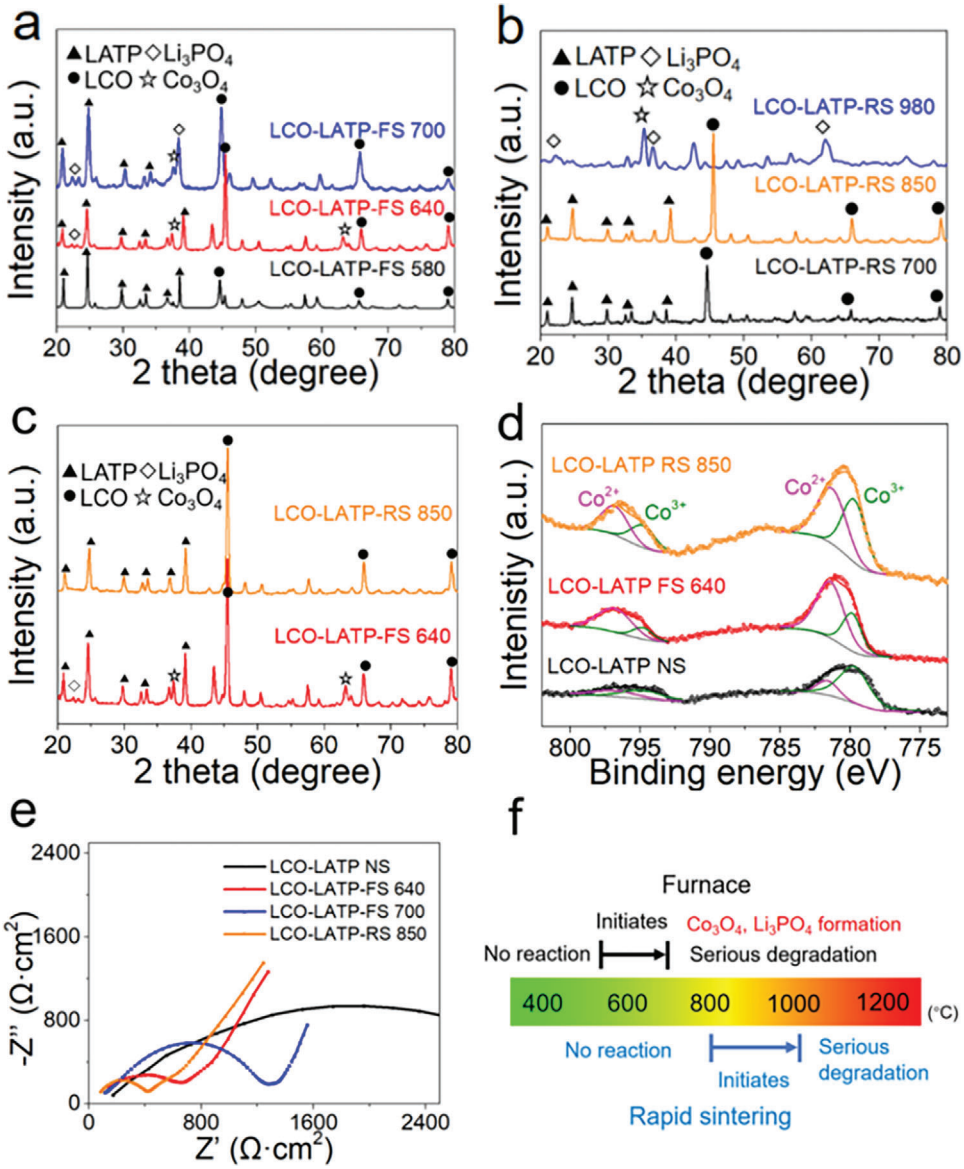


**Figure 2.** a) XRD powder patterns of LCO-LATP furnace sintered pellets at 580 °C (black), 640 °C (red), and 700 °C (blue). The corresponding peaks are marked with symbols. b) XRD powder patterns of LCO-LATP rapid sintered pellets at 700 °C (black), 850 °C (yellow), and 980 °C (blue). c) XRD powder patterns of LCO-LATP furnace sintered pellets at 640 °C (red) and LCO-LATP rapid sintered pellets at 850 °C (orange). d) XPS spectra of pristine LCO-LATP pellets (black), furnace sintered pellets at 640 °C (orange), LCO-LATP rapid sintered pellets at 850 °C (red). The peaks are deconvoluted into $Co^{3+}$ (green) and $Co^{2+}$ (pink). e) EIS of the LCO-LATP cells before and after sintering, tested at 25 °C. The curves are pristine LCO-LATP pellets (black), furnace sintered pellets at 640 °C (red), furnace sintered pellets at 700 °C (blue) and rapid sintered pellets at 800 °C (orange). f) Reactivity between LCO and LATP in furnace sintering and rapid sintering as related to the temperature.

formation of $Co_3O_4$ (Figure S9, Supporting Information). The pellets sintered at 640 °C in the furnace and rapid sintered at 850 °C were compared in Figure 2c. The LCO cathode pellet was further analyzed by the X-ray photoelectron spectroscopy (XPS) before and after the sintering. The spectra, presented in Figure 2d, were recorded, and deconvoluted to probe the Co oxidation states. According to the XPS results in previous studies,[53] the Co $2p_{3/2}$ peaks at 779.7 and 781.6 eV are assigned to $Co^{3+}$ and $Co^{2+}$ and the Co $2p_{1/2}$ peaks at 794.8 and 796.8 eV are assigned to $Co^{3+}$ and $Co^{2+}$, respectively. In the pristine LCO-LATP cathode which is not sintered (denoted as LCO-LATP NS), $Co^{3+}$ dominates. The $Co^{3+}$:$Co^{2+}$ ratio decreased significantly after furnace sintering at 640 °C due to the formation of $Co_3O_4$ species on the surface that was identified in the XRD (Figure 2a). In the rapid sintered at 850 °C (RS 850) sample, the $Co^{3+}$:$Co^{2+}$ ratio also decreased compared to the pristine sample, but the ratio is lower than the furnace sintered at 640 °C (FS 640) sample. The result suggests a more obvious $Co^{3+}$ reduction happens in the furnace sintering, which likely results in the thick insulating layer formation and the cathode capacity loss.

No side product between LCO and LATP was detected by XRD after rapid sintering at 850 °C while $Li_3PO_4$ and $Co_3O_4$ were

detected as a secondary phase after sintering at 640 °C in the furnace (Figure 2c). To determine the effect of grain and interphase formation on the interfacial contact at the cathode interface, the conductivity of LATP/LCO-LATP pellets was tested by electrochemical impedance spectroscopy (EIS). The LATP/LCO-LATP pellets were produce by the rapid sintering process and Ag paste was deposited on both sides of the discs as the block electrode. The pellets not sintered or sintered in the furnace at 640 and 700 °C (denoted as FS 640 and FS 700, respectively) were used for comparison (Figure 2e). From the equivalent circuit (Figure S10, Supporting Information), $R_{ct}$ is the charge transfer resistance and double layer capacitance on the LCO-LATP interfaces and $Z_w$ is for the diffusion impedance inside of the LCO-LATP cathode. The cell before thermal treatment exhibited high interfacial resistance, suggesting poor LCO-LATP contact. The furnace sintered cathode reduced the $R_{ct}$ to 700 Ω cm$^2$ at 640 °C. The results indicate that an ion-conductive interphase, such as $Li_3PO_4$ and $Co_3O_4$, formed in the furnace sintering process. $Li_3PO_4$ is reported to improve the Li-ion transport and possess an ionic conductivity of $10^{-6}$–$10^{-8}$ S cm$^{-1}$.[54,55] $Co_3O_4$ addition increased the ionic conductivity of composite polymer electrolytes and yttria-stabilized zirconia.[56,57] The results suggest the initial interphase between the layers is composed of partially crystallized $Li_3PO_4$ and $Co_3O_4$ before complete degradation of the LCO and LATP at higher temperature. The RS 850 sample has a $R_{ct}$ reduced to 400 Ω cm$^2$. The low resistance is due to the intimate contact and efficient $Li^+$ transfer in the formed interphase.

The reactivity between LATP and LCO and the difference of two sintering methods have been summarized in Figure 2f. In the furnace sintering method, the side reaction initiates at ≈500 °C and serious degradation is found >700 °C. In the transition region, the molar ratio of reaction species and interphase morphology is related to the particle size and sintering duration. The small particles are more susceptible to solid-phase reactions. The side products accumulate, and the thickness of the interphase increased during the sintering. These interfacial properties contribute to the ionic conductivity of the cathode. The thick interphase and serious interdiffusion degrades the performance of the cathode in SSBs. Here the pellet was sintered for 1 h in the furnace. It was found that the necessary temperature for intimate physical contact formation is ≈700 °C, while $Co_3O_4$ and $Li_3PO_4$ side products were observed at that temperature. This result demonstrates that it is challenging to form an active interface in the furnace. However, the reaction temperature window was extended to over 800 °C with the rapid sintering process. Due to the short annealing duration, the reaction was limited to the contact area and no reaction in the bulk material was detected up to 850 °C. Much degradation was detected over 980 °C. The high temperature significantly accelerated the solid-phase reaction between LATP and LCO and the decomposition was almost complete within ≈10 s. The differences of reactivity indicate that the thermodynamically favored reactions between LCO and LATP can be restricted by the reaction kinetics with rapid heating and cooling rates. The rapid sintering technique enables the study of this reaction at the timescale of seconds; the results suggest the reaction temperature plays a more important role than the reaction duration.

The ion-conductive interphase formation has a major effect on the behavior of the cathode. Conductive grain boundary growth requires high sintering temperature, which is at least 640 °C in the LCO-LATP system as determined by the furnace sintering conditions. The contact of LCO and LATP was observed in the SEM images before and after thermal treatment in **Figure 3**. The morphology of pristine hand-mixing LCO-LATP cathode is shown in Figure 3a. The poor point-to-point contact was caused by the rigid nature of LATP ceramic and LCO particles. The LATP framework itself is not continuous enough without the sintering treatment. An obvious gap of ≈0.5 µm can be identified by energy dispersive X-ray (EDX) analysis (Figure 3b). Co and Ti, P elements correspond to LCO and LATP, respectively. The lack of physical contact slows electron and ion transfer in the cathode. After at the process to produce RS 850, the contact between LATP-LATP, as well as LCO-LATP, was greatly enhanced (Figure 3d) and a ≈1 µm thick interphase was introduced between LCO and LATP particles. The intensity of Co decreased while the intensity of P and Ti increased in the transition layer. The counts of Ti overlap with P very well, which confirms the good stability of LATP in the rapid sintering process. In the FS 640 sample, intimate physical contact was also observed (Figure 3g). Due to the low sintering temperature, the LATP was not densely sintered. By comparison, the thickness of the transition layer is >2.5 µm (Figure 3h). This suggests high interdiffusion on the interface that might lead to capacity loss. The reaction models were shown in Figure 3c,f,i. The island-like LCO particles (shown in blue) are surrounded by the LATP network (shown in green). The particle distribution in the cathode composite was confirmed by SEM images (Figure S11, Supporting information). To reduce the gap and construct efficient $Li^+$ transfer pathways in the cathode (Figure 3c), an appropriate sintering treatment is necessary for the O-SEs. A long sintering process can form a good physical contact but the crystalline side product formation and deep interdiffusion lowers the overall cathode performance (Figure 3i). During the rapid sintering, a thinner interphase was formed at higher sintering temperature but with a much shorter duration (Figure 3f). The chemical composition of the layer cannot be identified by XRD, and it is more amorphous. The low-crystalline domain can be identified around the LCO particles in HRTEM images after rapid sintering at 850 °C (Figure S12, Supporting information). Based on the previous studies, the thin, amorphous interphase possesses a higher ionic conductivity compared to the thick, crystallized interphase in the O-SE systems.[58,59] The amorphous nature of the interphase introduced by rapid sintering might be beneficial to the transfer in the cathode pellets.

### 2.4. Electrochemical Performance of SSBs Containing the LCO-LATP Composite Cathodes

To evaluate the effects of interphase after treatment, the sintered cathodes were tested in the SSBs. Li metal was used as the anode and a PVDF-HFP layer (Figure S13, Supporting Information) was employed to avoid the LATP reduction against Li. The LCO active material mass loading is ≈10 mg cm$^{-2}$ and the charge/discharge rates are set to be 0.05 C (1 C = 130 mA g$^{-1}$). The battery can be reversibly charged and discharged between 2.8 and 4.2 V at 25 °C. The RS 800 cathode exhibited a high average CE of 99.8% and a capacity retention of 75% in the initial 200 cycles (**Figure 4**a). To our knowledge, the cycling stability is the highest in the

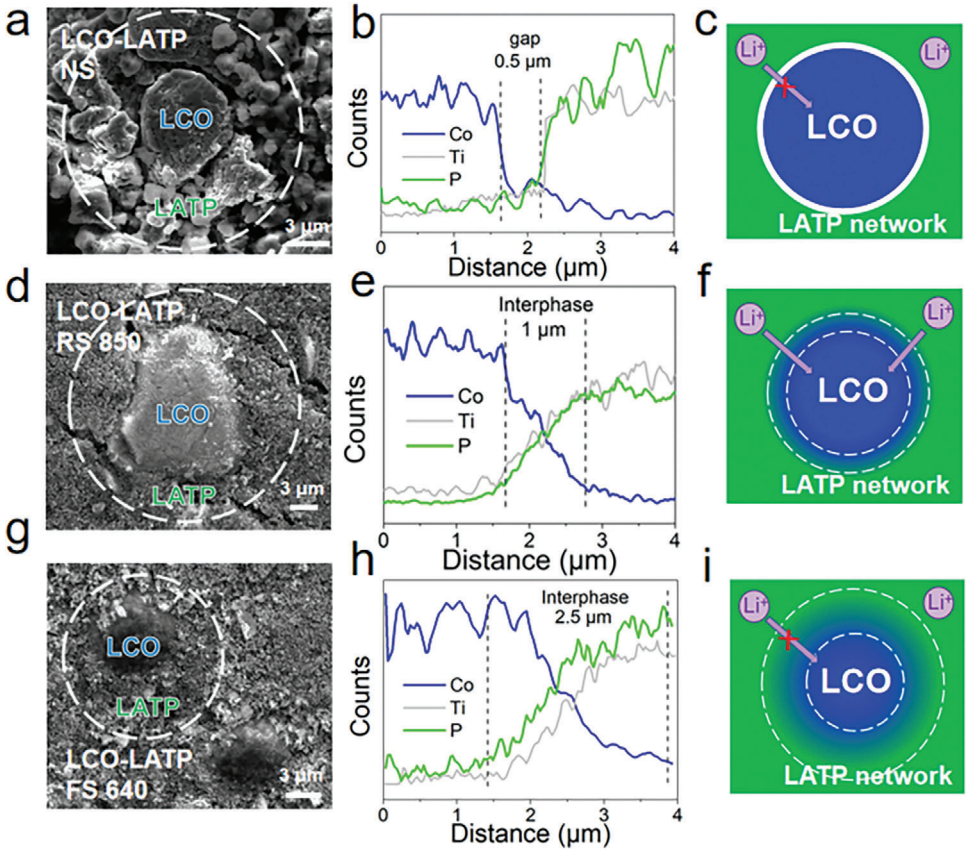


**Figure 3.** SEM images of a) pristine LCO-LATP, d) LCO-LATP rapid sintered pellets at 850 °C and g) LCO-LATP furnace sintered pellets at 640 °C. EDX elemental distribution on the LCO-LATP interface for b) pristine LCO-LATP, e) LCO-LATP rapid sintered pellets at 850 °C, and h) LCO-LATP furnace sintered pellets at 640 °C. Diagrams illustrating the proposed interfacial morphology for c) pristine LCO-LATP, f) LCO-LATP rapid sintered pellets at 850 °C and i) LCO-LATP furnace sintered pellets at 640 °C.

O-SE systems at room temperature and even at an elevated temperature (Table S1, Supporting Information). The LCO-LATP cathode shows typical capacity–voltage profiles (Figure 4b) and good reversibility at higher rates (Figure 4c). No obvious mechanical failure was detected after the cycling (Figure S14, Supporting Information). The results demonstrate the effectiveness of the rapid sintering strategy in constructing the amorphous interphase between LCO and LATP. It indicates the feasibility of long cycling of thick O-SE cathodes at room temperature by introducing an intimate and robust interphase. The capacities were compared in Figure 4d (recorded after 10 cycles after 0.05 C). The red curve suggests there is an obvious capacity loss in the furnace sintered cathode pellets if no sintering additive is added. The highest capacity was ≈60 mAh $g^{-1}$ in the FS 640 sample. The capacity trend of RS samples is shown in the black curve. Low sintering temperatures (700 and 750 °C) did not produce continuous contact and ion transfer channels, resulting in low capacities. If we assume the LCO cathode material did not decompose in the sintering, and the practical capacity is ≈140 mAh $g^{-1}$, the LCO utilization ratio was 10–30% in the poor-contact cathodes. Medium temperatures (800 and 850 °C) were effective to introduce a conductive interphase between LCO and LATP particles and the reaction was limited on the surface due to the short annealing duration. The initial capacities were over 120 mAh $g^{-1}$. When high temperatures (>900 °C) were applied to the cathode, the capacity decreased because of the side product accumulation and interdiffusion. The RS 980 sample showed almost no reversible capacity. The capacity plot indicates the precise temperature control is critical to achieve high capacity even in a shorter sintering process.

### 2.5. Applications of Rapid Sintering in NMC and LFP Cathodes

NMC and LFP cathode materials are possible candidates for use in batteries for electric vehicles. NMC features high voltage and high specific capacity while LFP provides lower cost and toxicity. To investigate the feasibility of the rapid sintering method in other common cathodes, rapidly sintered LFP and NMC811 composite cathodes were assembled and tested in the same configuration. The optimized sintering temperatures of NMC and LFP are 800 and 600 °C, respectively, which suggests that different conductive interphases can be successfully produced with the rapid sintering technique in other cathodes. The thermal stabilities of NMC and LFP with LATP are up to ≈600 and ≈450 °C, respectively, in the furnace. The rapid sintering method allows for the formation of an efficient interphase at higher temperature without oxidizing the bulk cathode. Similar resistance decrease behaviors are observed (Figures S15 and S16, Supporting

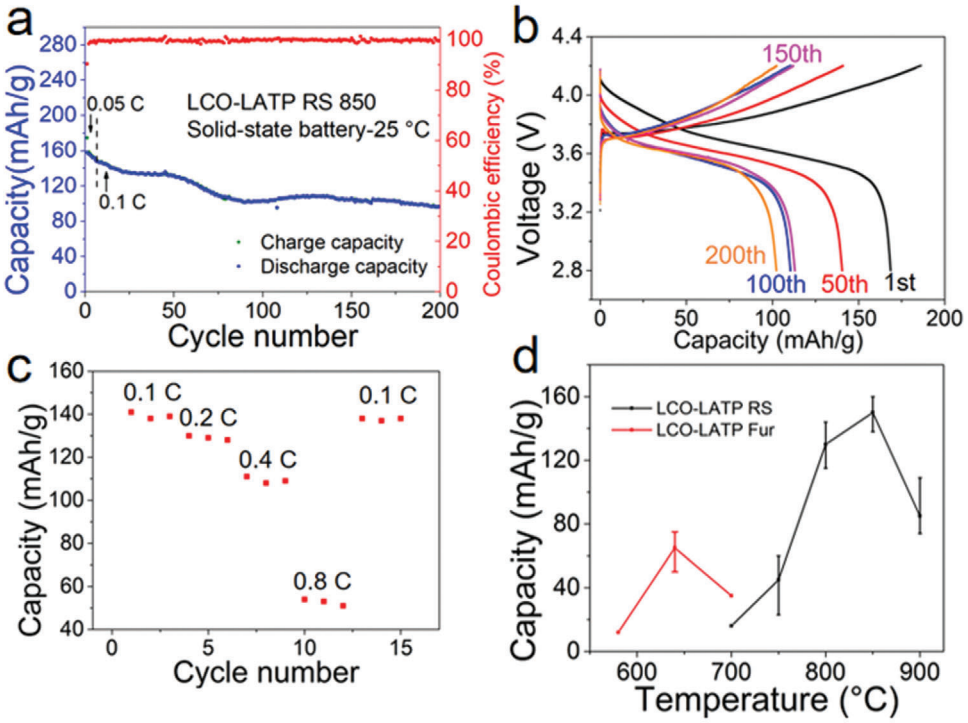


**Figure 4.** a) Cycling stability of rapid sintered LCO-LATP pellets at 850 °C. The LCO active material loading is ≈10 mg cm$^{-2}$ and the charge and discharge rates were set to 0.05 C (1 C = 130 mA g$^{-1}$) in a voltage range of 2.8–4.2 V. The initial areal capacity is ≈0.8 mAh cm$^{-2}$. b) Charge–discharge capacity–voltage profiles of LATP/LCO-LATP SSB. c) Rate performance of the LATP/LCO-LATP SSB. d) Comparison of specific capacity of LCO-LATP pellets at different sintering conditions; furnace sintering and rapid sintering pellets are shown in red and black, respectively.

Information). The cycling performance of NMC811 and LFP cathodes is shown in **Figure 5**. The SSB with NMC-LATP RS 800 cathode exhibited a capacity of ≈140 mAh g$^{-1}$ and can be cycled over 200 cycles with a high-capacity retention of 75% (Figure 5a). The capacity–voltage curve shows a typical NMC character and the activation behavior in the initial 10 cycles was observed. Similarly, LFP exhibited a high capacity of 140 mAh g$^{-1}$ at a range of 2.0–3.7 V (Figure 5d). The reversible charge and discharge behavior was also noticed below 2.8 V due to the formation of a redox species during sintering. The extra reversible capacity was also noticed in previous research on a LFP-LATP system.[59] The thermal stabilities of NMC and LFP cathodes during sintering are summarized in Figure 5c,f. The rapid sintering method has extended the sintering window from 600 to 800 °C for NMC and 400 to 600 °C for LFP. The lower thermal stability of LFP compared to NMC and LCO is likely due to its intrinsic stability and a smaller particle size. The characterization data of NMC-LATP and LFP-LATP cathodes are shown (Figures S17 and S21, Supporting Information). Continuous interphase formation between LATP and NMC/LFP particles can be noticed after the rapid sintering process while no obvious side products were identified in the XRD patterns. The high reversible capacities of SSBs with various rapid sintered cathode demonstrates that the rapid sintering technique is a general method for introducing a conductive interphase without any sintering additive.

## 3. Conclusion

In summary, we developed a solvent-free method to construct a stable oxide solid electrolyte cathode interface under ambient conditions. The amorphous transition layer induced by rapid sintering reduced the interfacial charge transfer resistance. The reaction temperature has been raised from 640 °C in the furnace to 850 °C during the rapid sintering process, without degradation. The reaction initiates on the edges and no obvious cathode material degradation was observed. The method can be applied to different cathode active materials. SSB with LCO-LATP composite cathodes charge and discharge reversibly at a high mass capacity ≈120 mAh g$^{-1}$ and areal capacity 0.5–1.0 mAh over 200 cycles. The rapid sintering method is also applicable in constructing conductive interphases in the NMC and LFP cathodes. This work provides a general method to fabricate SSBs with NASICON solid electrolyte and cathode materials in a low-cost, scalable way.

## 4. Experimental Section

*Materials*: $Li_2CO_3$ (99.0 wt%, Millipore-Sigma), $Al_2O_3$ (<50 nm particle size, Millipore-Sigma), $TiO_2$ (99.8 wt%, Millipore-Sigma) and $NH_4H_2PO_4$ (98.5 wt%, Millipore-Sigma) precursors were used to synthesize the LATP solid electrolyte. Poly(vinylidene fluoride-co-hexafluoropropylene) (PVDF-HFP), 1-methyl-2-pyrrolidinone (NMP, 99.5 wt%, Millipore-Sigma), bis(trifluoromethane)sulfonimide lithium (LiTFSI) salt (99.95 wt%, Millipore-Sigma), and tetraethylene glycol

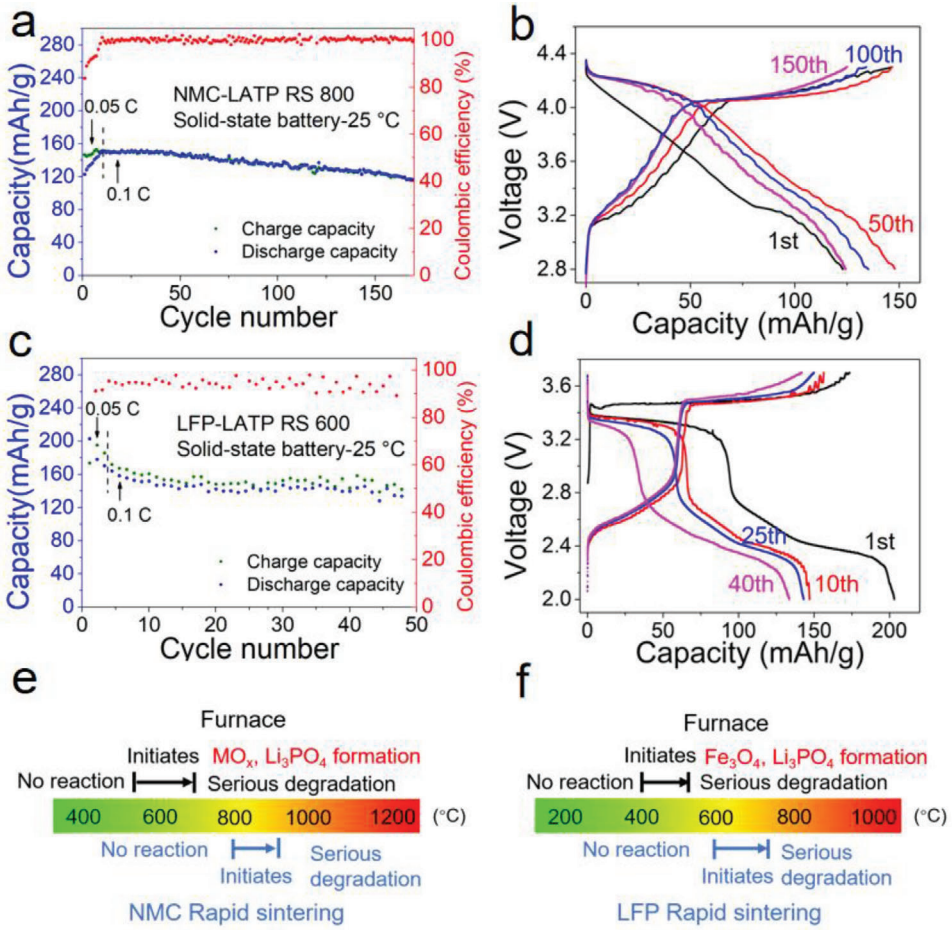


**Figure 5.** a) Cycling stability of rapid sintered NMC-LATP pellets at 800 °C. The cells were tested at 25 °C. b) Charge–discharge capacity–voltage profiles of the LATP/NMC-LATP SSB. c) Cycling stability of rapid sintered LFP-LATP pellets at 800 °C. The cells were tested at 25 °C. d) Charge–discharge capacity–voltage profiles of the LATP/LFP-LATP SSB. e) Reactivity between NMC and LATP in furnace sintering and rapid sintering in relation to the temperature. f) Reactivity between LFP and LATP in furnace sintering and rapid sintering in relation to the temperature.

dimethyl ether (TEGDME) were used for the PVDF-HFP membrane fabrication. LCO (99.8 wt%, Millipore-Sigma), NMC811 (Single crystal, MTI corporation), LFP (MTI corporation) were used as the cathode materials. Highly conductive acetylene black (ABHC-01, Soltex Corporation) was used as the conductive additive in the cathode. Lithium chips ($D = 16$ mm, $t = 0.6$ mm, 99.9 wt%, MTI Corporation) were used as the anode of SSBs.

*LATP Synthesis*: The LATP solid electrolyte was synthesized by heating the $Li_2CO_3$, $Al_2O_3$, $TiO_2$, and $NH_4H_2PO_4$ precursors. The precursor powders were mixed in a stoichiometric ratio, except that 10% $Li_2CO_3$ excess was used to mitigate Li loss, and ball-milled for 6 h with isopropyl alcohol. Then the mixture was dried and heated at 850 °C for 12 h. The obtained LATP powder was ball-milled for 6 h with isopropyl alcohol and dried.

*Cathode Pellet Preparation*: The obtained LATP powder was pressed into pellets (3 ton, ≈150 MPa) with a 15 mm Pellet Press Die Set (purchased from Pellet Press Die Sets). The pellet was annealed with the rapid sintering device at 980 °C for 30 s. The mixed cathode powder, consisting of 70% LCO (or LFP or NMC), 27% LATP, and 3% acetylene black was hand mixed for 30 min. The mixture was sprayed onto the LATP pellet and pressed again (3 ton, ≈150 MPa).

*Furnace Sintering Process*: The double-layer SE-cathode was placed in a $Al_2O_3$ crucible and heated to the target temperature with a heating rate of 20 °C $min^{-1}$ and a cooling rate of 5 °C $min^{-1}$. The pellet was kept at target temperature for 1 h.

*Rapid Sintering Process*: The electric diagram of the rapid sintering system is shown in Figure S1a (Supporting Information). The total capacitance of the capacitor bank is 1.5 F. The system was capable of charging to a voltage of 0–63 V and a current of 0–100 A. Two carbon papers (Toray Carbon Paper 060, FuelCellStore) attached to a glass slide were used as the heating element and sample holder (Figure S1b,c, Supporting Information). The temperature was controlled by changing the resistance of the carbon papers. The pellets were put in between the carbon papers, which were connected to the rapid sintering system. The voltage was set to ≈15 V and the sintering time was 5 s. Two pulses were applied on the sample.

*Electrochemical Performance Measurements*: 20 µL of 4 mg $mL^{-1}$ acetylene black suspension in NMP was dropped onto the cathode material side and dried overnight in the oven. The cathode pellet was placed on a thin PVDF-HFP polymer layer (Figure S13, Supporting Information). The membrane was rinsed with 1 M LiTFSI in TEGDME, dried with a Kimwipe before assembly. A Li metal foil was used as the anode. The electrode was then pressed and sealed in a 2032-type coin cell inside an Ar-filled glovebox ($O_2$ content <0.5 ppm, $H_2O$ content <0.5 ppm). Electrochemical impedance spectroscopy (EIS) was measured at room temperature between 100 kHz and 0.01 Hz with an amplitude of 10 mV. The coin-cells were charged and discharged on a battery working station (LANHE Corporation, China) in air at 25 °C.

*Characterizations*: XRD was performed by the Rigaku SmartLab system with a filtered Cu K$\alpha$ radiation ($\lambda = 1.5406$ Å). XPS spectra were taken by the PHI Quantera XPS system under a pressure of $5 \times 10^{-9}$ Torr. The survey spectra were collected with a step size of 0.5 eV and a pass energy of 140 eV, and elemental spectra were collected with a step size of 0.1 eV and a pass energy of 26 eV. All XPS spectra were calibrated using the C 1*s* peak at 284.8 eV as the reference. The SEM images and element analysis by EDS were taken on the FEI Helios NanoLab 660 DualBeam SEM system under a voltage of 10 kV and a working distance of 10 mm.

## Supporting Information

Supporting Information is available from the Wiley Online Library or from the author.

## Acknowledgements

The authors thank Dr. Bo Chen of Rice University for helpful discussion on the XPS results. The funding of the research is provided by Air Force Office of Scientific Research (FA9550-22-1-0526). The authors acknowledge the use of the Electron Microscopy Center (EMC) at Rice University. The characterization equipment used in this project is from the Shared Equipment Authority (SEA) at Rice University.

## Conflict of Interest

The authors declare no conflict of interest.

## Author Contributions

J.C. conceived the idea, designed the experiments, and conducted the characterizations. W.C. contributed to the experimental design and electrochemical measurement. B.D. and C.K. helped to build the rapid sintering device. J.C. and J.M.T. wrote and edited the manuscript. All aspects of the research were overseen by J.M.T. All authors discussed the results and commented on the manuscript.

## Data Availability Statement

The data that support the findings of this study are available in the Supporting Information of this article.

## Keywords

cathode interface, co-sintering, LATP, oxide-based solid electrolytes, solid-state batteries

Received: August 23, 2023
Published online: October 11, 2023

[1] R. Chen, Q. Li, X. Yu, L. Chen, H. Li, *Chem. Rev.* **2020**, *120*, 6820.
[2] M. Balaish, J. C. Gonzalez-Rosillo, K. J. Kim, Y. Zhu, Z. D. Hood, J. L. M. Rupp, *Nat. Energy* **2021**, *6*, 227.
[3] K. J. Kim, M. Balaish, M. Wadaguchi, L. Kong, J. L. M. Rupp, *Adv. Energy Mater.* **2021**, *11*, 2002689.
[4] C. Li, Z.-Y. Wang, Z.-J. He, Y.-J. Li, J. Mao, K.-H. Dai, C. Yan, J.-C. Zheng, *Sustainable Mater. Technol.* **2021**, *29*, e00297.
[5] Q. Zhang, D. Cao, Y. Ma, A. Natan, P. Aurora, H. Zhu, *Adv. Mater.* **2019**, *31*, 1901131.
[6] C. Wang, J. Liang, Y. Zhao, M. Zheng, X. Li, X. Sun, *Energy Environ. Sci.* **2021**, *14*, 2577.
[7] D. Zeng, J. Yao, L. Zhang, R. Xu, S. Wang, X. Yan, C. Yu, L. Wang, *Nat. Commun.* **2022**, *13*, 1909.
[8] Y. Lee, J. Jeong, H. J. Lee, M. Kim, D. Han, H. Kim, J. M. Yuk, K.-W. Nam, K. Y. Chung, H.-G. Jung, S. Yu, *ACS Energy Lett.* **2022**, *7*, 171.
[9] H. Liu, Y. Liang, C. Wang, D. Li, X. Yan, C.-W. Nan, L.-Z. Fan, *Adv. Mater.* **2022**, https://doi.org/10.1002/adma.202206013.
[10] L. Xu, J. Li, W. Deng, H. Shuai, S. Li, Z. Xu, J. Li, H. Hou, H. Peng, G. Zou, X. Ji, *Adv. Energy Mater.* **2021**, *11*, 2000648.
[11] K. Yang, L. Chen, J. Ma, Y.-B. He, F. Kang, *InfoMat* **2021**, *3*, 1195.
[12] R. Dewees, H. Wang, *ChemSusChem* **2019**, *12*, 3713.
[13] Q. Cheng, A. Li, N. Li, S. Li, A. Zangiabadi, T.-D. Li, W. Huang, A. C. Li, T. Jin, Q. Song, W. Xu, N. Ni, H. Zhai, M. Dontigny, K. Zaghib, X. Chuan, D. Su, K. Yan, Y. Yang, *Joule* **2019**, *3*, 1510.
[14] L. He, W.-H. Liang, J.-H. Cao, D.-Y. Wu, *ACS Appl. Energy Mater.* **2022**, *5*, 5277.
[15] C. Wang, K. Fu, S. P. Kammampata, D. W. Mcowen, A. J. Samson, L. Zhang, G. T. Hitz, A. M. Nolan, E. D. Wachsman, Y. Mo, V. Thangadurai, L. Hu, *Chem. Rev.* **2020**, *120*, 4257.
[16] N. Zhao, W. Khokhar, Z. Bi, C. Shi, X. Guo, L.-Z. Fan, C.-W. Nan, *Joule* **2019**, *3*, 1190.
[17] S. Abouali, C.-H. Yim, A. Merati, Y. Abu-Lebdeh, V. Thangadurai, *ACS Energy Lett.* **2021**, *6*, 1920.
[18] H. Huo, J. Luo, V. Thangadurai, X. Guo, C.-W. Nan, X. Sun, *ACS Energy Lett.* **2020**, *5*, 252.
[19] K. (K.) Fu, Y. Gong, Z. Fu, H. Xie, Y. Yao, B. Liu, M. Carter, E. Wachsman, L. Hu, *Angew. Chem., Int. Ed. Engl.* **2017**, *56*, 14942.
[20] X.-D. Zhang, F.-S. Yue, J.-Y. Liang, J.-L. Shi, H. Li, Y.u-G. Guo, *Small Struct.* **2020**, *1*, 2000042.
[21] R. Schlem, C. F. Burmeister, P. Michalowski, S. Ohno, G. F. Dewald, A. Kwade, W. G. Zeier, *Adv. Energy Mater.* **2021**, *11*, 2101022.
[22] L. Ye, X. Li, *Nature* **2021**, *593*, 218.
[23] Z. Zhang, S. Chen, J. Yang, J. Wang, L. Yao, X. Yao, P. Cui, X. Xu, *ACS Appl. Mater. Interfaces* **2018**, *10*, 2556.
[24] C. Wang, Y. Gong, B. Liu, K. Fu, Y. Yao, E. Hitz, Y. Li, J. Dai, S. Xu, W. Luo, E. D. Wachsman, L. Hu, *Nano Lett.* **2017**, *17*, 565.
[25] H. Xu, Y. Li, A. Zhou, N. Wu, S. Xin, Z. Li, J. B. Goodenough, *Nano Lett.* **2018**, *18*, 7414.
[26] Y. Li, Y. Sun, A. Pei, K. Chen, A. Vailionis, Y. Li, G. Zheng, J. Sun, Y. Cui, *ACS Cent. Sci.* **2018**, *4*, 97.
[27] Y. Zhu, X. He, Y. Mo, *ACS Appl. Mater. Interfaces* **2015**, *7*, 23685.
[28] Y. Liu, Q. Sun, Y. Zhao, B. Wang, P. Kaghazchi, K. R. Adair, R. Li, C. Zhang, J. Liu, L.-Y. Kuo, Y. Hu, T.-K. Sham, L. Zhang, R. Yang, S. Lu, X. Song, X. Sun, *ACS Appl. Mater. Interfaces* **2018**, *10*, 31240.
[29] X. Hao, Q. Zhao, S. Su, S. Zhang, J. Ma, L. Shen, Q. Yu, L. Zhao, Y. Liu, F. Kang, Y.-B. He, *Adv. Energy Mater.* **2019**, *9*, 1901604.
[30] A. Banerjee, X. Wang, C. Fang, E. A. Wu, Y. S. Meng, *Chem. Rev.* **2020**, *120*, 6878.
[31] W. D. Richards, L. J. Miara, Y. Wang, J. C. Kim, G. Ceder, *Chem. Mater.* **2016**, *28*, 266.
[32] S. Lou, F. Zhang, C. Fu, M. Chen, Y. Ma, G. Yin, J. Wang, *Adv. Mater.* **2021**, *33*, 2000721.
[33] Q. Zhao, S. Stalin, C.-Z. Zhao, L. A. Archer, *Nat. Rev. Mater.* **2020**, *5*, 229.
[34] Z. Bi, N. Zhao, L. Ma, Z. Fu, F. Xu, C. Wang, X. Guo, *Chem. Eng. J.* **2020**, *387*, 124089.
[35] S. A. Pervez, M. A. Cambaz, V. Thangadurai, M. Fichtner, *ACS Appl. Mater. Interfaces* **2019**, *11*, 22029.
[36] X. Yu, A. Manthiram, *ACS Appl. Energy Mater.* **2020**, *3*, 2916.

[37] L. Chen, Y. Li, S.-P. Li, L.-Z. Fan, C.-W. Nan, J. B. Goodenough, *Nano Energy* **2018**, *46*, 176.
[38] H. Xie, C. Yang, K. (K.) Fu, Y. Yao, F. Jiang, E. Hitz, B. Liu, S. Wang, L. Hu, *Adv. Energy Mater.* **2018**, *8*, 1703474.
[39] T. Kato, T. Hamanaka, K. Yamamoto, T. Hirayama, F. Sagane, M. Motoyama, Y. Iriyama, *J. Power Sources* **2014**, *260*, 292.
[40] M. Kotobuki, K. Kanamura, Y. Sato, T. Yoshida, *J. Power Sources* **2011**, *196*, 7750.
[41] H.-S. Kim, Y. Oh, K. H. Kang, J. H. Kim, J. Kim, C. S. Yoon, *ACS Appl. Mater. Interfaces* **2017**, *9*, 16063.
[42] F. Ichihara, S. Miyoshi, T. Masuda, *Phys. Chem. Chem. Phys.* **2022**, *24*, 25878.
[43] M. Malaki, A. Pokle, S.-K. Otto, A. Henss, J. P. Beaupain, A. Beyer, J. Müller, B. Butz, K. Wätzig, M. Kusnezoff, J. Janek, K. Volz, *ACS Appl. Energy Mater.* **2022**, *5*, 4651.
[44] J. P. Beaupain, K. Waetzig, S.-K. Otto, A. Henss, J. Janek, M. Malaki, A. Pokle, J. Müller, B. Butz, K. Volz, M. Kusnezoff, A. Michaelis, *ACS Appl. Mater. Interfaces* **2021**, *13*, 47488.
[45] M. Gellert, E. Dashjav, D. Grüner, Q. Ma, F. Tietz, *Ionics (Kiel)* **2018**, *24*, 1001.
[46] C.-Y. Yu, J. Choi, V. Anandan, J.-H. Kim, *J. Phys. Chem. C: Nanomater. Interfaces* **2020**, *124*, 14963.
[47] K. Park, B.-C. Yu, J.-W. Jung, Y. Li, W. Zhou, H. Gao, S. Son, J. B. Goodenough, *Chem. Mater.* **2016**, *28*, 8051.
[48] X. Han, S. Wang, Y. Xu, G. Zhong, Y. Zhou, B. Liu, X. Jiang, X. Wang, Y. Li, Z. Zhang, S. Chen, C. Wang, Y. Yang, W. Zhang, J. Wang, J. Liu, J. Yang, *Energy Environ. Sci.* **2021**, *14*, 5044.
[49] K. Homma, Y. Liu, M. Sumita, R. Tamura, N. Fushimi, J. Iwata, K. Tsuda, C. Kaneta, *J. Phys. Chem. C: Nanomater. Interfaces* **2020**, *124*, 12865.
[50] B. Liu, K. Fu, Y. Gong, C. Yang, Y. Yao, Y. Wang, C. Wang, Y. Kuang, G. Pastel, H. Xie, E. D. Wachsman, L. Hu, *Nano Lett.* **2017**, *17*, 4917.
[51] B. Deng, P. A. Advincula, D. X. Luong, J. Zhou, B. Zhang, Z. Wang, E. A. Mchugh, J. Chen, R. A. Carter, C. Kittrell, J. Lou, Y. Zhao, B. I. Yakobson, Y. Zhao, J. M. Tour, *Nat. Commun.* **2022**, *13*, 5027.
[52] E. Antolini, M. Ferretti, *J. Solid State Chem.* **1995**, *117*, 1.
[53] C. Alex, S. C. Sarma, S. C. Peter, N. S. John, *ACS Appl. Energy Mater.* **2020**, *3*, 5439.
[54] X. Liu, Q. Weng, T. Liu, Z. Tang, H. Tang, *Electrochim. Acta* **2023**, *447*, 142151.
[55] Y.-Q. Sun, X.-T. Luo, Y.-S. Zhu, X.-J. Liao, C.-J. Li, *J. Eur. Ceram. Soc.* **2022**, *42*, 4239.
[56] Q. Zhou, S. Liu, S. Zhang, Y. Che, L.-H. Gan, *Front. Mater.* **2021**, *8*, https://doi.org/10.3389/fmats.2021.697257.
[57] B. Aktas, S. Tekeli, *Int. J. Mater. Res. (Z. Metallkd.)* **2014**, *105*, 577.
[58] Y. Gao, S. Sun, X. Zhang, Y. Liu, J. Hu, Z. Huang, M. Gao, H. Pan, *Adv. Funct. Mater.* **2021**, *31*, 2009692.
[59] Q. Xu, Z. Liu, A. Windmüller, S. Basak, J. Park, K. Dzieciol, C.-L. Tsai, S. Yu, H. Tempel, H. Kungl, R.-A. Eichel, *Small* **2022**, *18*, e2200266.